

Influence of the porous texture of SBA-15 mesoporous silica on the anatase formation in TiO 2 –SiO 2 nanocomposites

Manon Besançon, Laure Michelin, Ludovic Josien, Loic Vidal, Karine Assaker, Magali Bonne, Bénédicte Lebeau, Jean-Luc Blin

▶ **To cite this version:**

Manon Besançon, Laure Michelin, Ludovic Josien, Loic Vidal, Karine Assaker, et al.. Influence of the porous texture of SBA-15 mesoporous silica on the anatase formation in TiO 2 –SiO 2 nanocomposites. New Journal of Chemistry, 2016, 40 (5), pp.4386-4397. 10.1039/C5NJ02859K . hal-03604865

HAL Id: hal-03604865
https://hal.science/hal-03604865

Submitted on 10 Mar 2022

HAL is a multi-disciplinary open access archive for the deposit and dissemination of scientific research documents, whether they are published or not. The documents may come from teaching and research institutions in France or abroad, or from public or private research centers.

L'archive ouverte pluridisciplinaire **HAL**, est destinée au dépôt et à la diffusion de documents scientifiques de niveau recherche, publiés ou non, émanant des établissements d'enseignement et de recherche français ou étrangers, des laboratoires publics ou privés.

Influence of the porous texture of SBA-15 mesoporous silica on the anatase formation in TiO_2 – SiO_2 nanocomposites

Manon Besançon,[a] Laure Michelin,[a] Ludovic Josien,[a] Loic Vidal,[a] Karine Assaker,[b] Magali Bonne,*[a] Bénédicte Lebeau,*[a] Jean-Luc Blin[b]

[a]Université de Haute Alsace, CNRS, Equipe Matériaux à Porosité Contrôlée, Institut de Science des Matériaux de Mulhouse, UMR 7361, ENSCMu, 3bis rue Alfred Werner, F-68093 Mulhouse cedex, France. E-mail: magali.bonne@uha.fr, benedicte.lebeau@uha.fr

[b]SRSMC UMR 7565, Université de Lorraine, CNRS, F-54506 Vandoeuvre-lès-Nancy cedex, BP 70239, France. E-mail: jean-luc.blin@univ.lorraine.fr

Abstract

Two series of TiO_2 – SiO_2 composites have been prepared by post-synthesis impregnation of a TiO_2 precursor onto SBA-15 silica matrices and a subsequent thermal treatment at 400 °C under air. The influence of the textural properties of the SBA-15 and the TiO_2 content on the dispersion of TiO_2 and its crystallization in anatase were evaluated. The morphology of the samples before and after impregnation was observed by electronic microscopy while the textural and structural properties were evaluated by different techniques such as XRD, nitrogen sorption manometry, Raman spectroscopy. The quantity of crystallized anatase in the composites was determined by a XRD quantification using an internal standard. The photocatylic properties of all composites were also studied by following the degradation of methyl orange (MO) in water under UV irradiation. For the same amount of catalyst, the MO degradation rate in presence of the composites containing 28 and 44 wt% of crystallized anatase was found similar to the one in the presence of a commercial fully crystallized anatase.

Introduction

Nowadays, the increasing interest in heterogeneous photocatalysis leads to the study and development of new photocatalysts. Indeed, water and air treatments, bacterial studies ... using photocatalysis are more and more developed[1-3]. Among all the photocatalysts studied, TiO_2 semi-conductor is one of the most used[4]. Titania exists as different polymorphs, the most known are brookite, anatase and rutile phases, presenting different physical properties[5]. Among these common crystalline forms of titania, due to its strong oxidizing properties and long term photostability, anatase is generally recognized to be the most active phase for photocatalysis[6,7]. Photocatalytic efficiency is favored by an increase of the crystalline degree, the particle size, the specific surface area and the porosity[8,9].

To enhance the photocatalytic activity of titania, different studies have been developed where titania is doped with metal ions or where mixed oxides are synthesized[10-12]. In particular, TiO_2 – SiO_2 mixed oxides exhibit a high thermal stability and mechanical strength; both properties come from silica, as well as good optical and catalytic properties, provided by the TiO_2 phase., In particular due to its properties such as high specific surface area, mesostructured silica is an excellent candidate as host support for titania. In addition to its textural properties, mesostructured silica is thermally stable and so can be used in many application fields. By this way, the advantages of the silica support (e.g. opened porosity, thermal stability) and the properties of Ti clusters are combined in order to improve the catalytic activity of TiO_2. Another advantage of the TiO_2 - SiO_2 mixed oxides concerns the delay in the anatase to rutile phase transition[13,14]. The use of a silica host support thus appears as an alternative way to nanostructure titania for catalytic applications. Indeed, lots of studies are developed in order to synthesize nanotubes of TiO_2 or mesoporous TiO_2 for increasing the titania specific surface area or to make possible the introduction of an active phase in the pores[15-18]. However, compared to silica materials it is difficult to obtain TiO_2 with stable mesostructure and the main challenge is to preserve the pore ordering upon surfactant removal. The other key parameter for the formation of titania with a mesopore ordering concerns the control of the titanium precursor hydrolysis and condensation as well as the aging process. As a matter of fact precursors such as titanium alkoxides or titanium chloride exhibit a high reactivity towards hydrolysis and condensation. As a consequence, dense TiO_2 with a poor mesopore arrangement is often recovered.

TiO_2 – SiO_2 mixed oxides have been prepared according to different methods: by sol-gel process with co-condensation of titania and silica sources[19-24] or by different post grafting processes[25-30]. For example, Lihitkar *et al.* have obtained TiO_2 nanoparticles embedded within the MCM-41 mesopores by the impregnation method[27]. The authors have reported that titania particles of an average size of 3 nm are obtained and that the titania particles are coordinated with silica MCM-41 by Si-O-Ti covalent bond.

For direct incorporation of Ti atoms in the silica walls during the synthesis, it is important to control the synthesis conditions and thus avoid the formation of large external Ti particles. For example, Zhao *et al.* have shown that at low content, titanium is incorporated into the framework of SBA-15. With the increase of titanium content, the TiO_2 anatase particles are formed, located on the external surface of SBA-15. The recovered Ti-SBA-15 composites are active for a photocatalytic reaction in water treatment[31].

By post-grafting TiO_2 on a SiO_2 host support, special attention should be paid to the loading amount of TiO_2 to avoid the pore blocking. It has been demonstrated that incorporation of TiO_2 at low loadings leads to good dispersion of Ti atoms in pore structure, and that the catalytic activity depends on the size of formed TiO_2 clusters. Comparing the direct and the post synthesis methods, the first one results in a relatively homogeneous incorporation of the titanium, whereas the post synthesis procedure leads to an increase of the titanium concentration on the surface[25].

Thanks to their characteristics, these oxides were used as good photocatalysts as well as support material for other heterogeneous catalysts[32-37]. Indeed, many researchers have reported on the preparation and properties of selective catalytic oxidation of various Ti-containing mesoporous materials, such as Ti-MCM-41[38,39], Ti-MCM-48[40], Ti-SBA-15[41], Ti-HMS[42], ... More recently, the impact of TiO_2 dispersed in a silica SBA-15 support and its influence on the activity of the CoMo catalysts in the hydrodesulfurization reaction were studied. An intermediate TiO_2 content of 20 wt% was determined to optimize active phase particles dispersion on the support and preserve intrinsic activity of the active sites[37].

In particular, the use of SBA-15 mesoporous silica as a host support for preparation of SiO_2 – TiO_2 composites has been largely studied and described in the literature[43-47] and their photocatalytic activity have been studied[48-51]. Indeed, in recent developments of photocatalytic materials regarding semiconductor TiO_2, metallic nanostructures in mesoporous silica frameworks were suggested for environmental remediation and solar energy utilization. The advantages of mesoporous-silica-based hosts are numerous, but the main important could be: 1) a large nanospace provided; 2) anchoring functional groups and moieties in order to create a unique photocatalytic reactor; 3) possible control of the diffusion, nanostructures, and sizes for the photo-responsive components[52].

In this work, different TiO_2 – SiO_2 composites were prepared by dispersing TiO_2 in SBA-15 type mesoporous silica. The choice of SBA-15 mesoporous silica as host support has been made because of the mesopores diameter which is in the range of 5 – 10 nm and also because it exhibits better thermal and hydrothermal stability compared to MCM-41 mesoporous silica. Composites of different TiO_2/SiO_2 mass ratios were prepared using a large pore SBA-15 host support, but also composites with the same TiO_2/SiO_2 mass ratios using SBA-15 host supports with different pore diameters. All the composites were prepared by post impregnation of SBA-15 support using a TiO_2 precursor diluted in alcohol and a subsequent thermal treatment at 400 °C under air. The materials were then finely characterized in order to have a precise description of the composites[13]. The objective of the study is to obtain nano particles of titania well dispersed inside the porosity of the silica support. The influence of the mean pore size of the supports is studied and the ~~The~~ quantity of crystallized anatase in each sample was determined by XRD quantification using an internal standard. This original method allows us to measure the quantity of anatase formed during the calcination process which can be different from the initial quantity of Ti precursor impregnated. Moreover, this quantification will allow us to correlate the influence of the use of the silica host support with the formation of anatase nanocrystals. Finally, the possible catalytic activity of the composites was evaluated by studying the photodegradation of methyl orange (MO) in water under UV irradiation.

Experimental part

Syntheses

1/ Synthesis of the host supports (SBA-15).

Triblock copolymer P123 $(EO)_{20}(PO)_{70}(EO)_{20}$ used as structure directing agent was purchased from Aldrich. TetraEthylOrthoSilicate (TEOS) and Titanium Isopropoxide ($Ti(O^iPr)_4$) from Aldrich were used as inorganic precursors. The SBA-15 supports were synthesized according to the protocol described by Zhao *et al.*[53]. In a polypropylene bottle, P123 was dissolved in an acidic medium of concentrated hydrochloric acid and water. The bottle was placed in a water bath at 40 °C in order to allow a complete dissolution of P123. Then TEOS was added by maintaining the temperature conditions. The molar composition of the gel was 1 TEOS: 0.017 P123: 5.68 HCl: 197 H_2O. The solution was stirred during 2 hours under these conditions and then transferred to the oven for an ageing step of 24 hours at a temperature comprised between 36 and 90 °C or transferred in an autoclave for an ageing step of 24 hours at

130 °C. After filtration and washing on a Buchner funnel the solid was dried at 70 °C for 24 hours. In order to release the porosity, the solid was calcined in a muffle furnace at 300 °C for 4 hours (temperature increasing time: 6 hours). Four different supports were synthesized at ageing temperatures of 36, 60, 90 and 130 °C for the different composites.

2/ TiO_2 – SiO_2 composite synthesis

Two series of TiO_2-SiO_2 composites have been prepared. The series a corresponds to composites made with 50 wt% of TiO_2 from SiO_2 SBA-15 hosts synthesized at 36, 60, 90 and 130 °C. The series b consists in composites with different TiO_2 loadings of 10, 25, 50, 70 and 80 wt% prepared from the same SiO_2 SBA-15 host synthesized at 130 °C. The different composites were prepared by impregnation in an excess of solvent. A known volume (depending on the desired titania loading) of $Ti(O^iPr)_4$ was diluted in 20 mL of dry ethanol and slowly added to the silica support in order to prepare 1 g of TiO_2 – SiO_2 composite. The solvent is evaporated under stirring at room temperature and the solid is dried at 70 °C for one night. For TiO_2 content superior to 50 wt% the impregnation procedure is repeated a second time to obtain the desired TiO_2 content. The TiO_2 loading vary from 10 to 80 wt%. The composite is then calcined at 400 °C under air during 4 hours (temperature increasing time: 6 hours) in order to obtain the anatase phase.

The nomenclature used for the composites is defined as follows:

XTin@Y

with: X = TiO_2 content (in wt%), Y = ageing temperature (°C) and n = a or b series.

It is noteworthy that two composites with 50 wt% of TiO_2 and a host support aged at 130 °C have been prepared: 50Tia@130 and 50Tib@130.

Materials characterization

The morphology of the supports and the composites as well as the Ti and Si distributions were observed by Scanning Electron Microscopy (Philips FEG XL30) coupled with Energy Dispersive X-ray Spectroscopy (EDS). The samples were first metalized by a thin carbon layer.

The pore structure of the different samples, as well as TiO_2 nanoparticles, were observed by Transmission Electronic Microscopy (TEM). Micrographs were obtained using a Philips CM200 working at 200 kV.

Powder low- and wide-angle XRD patterns were recorded on a PANalytical X'Pert Pro (45kV, 40mA) using a Cu Kα (λ = 1.5418 Å) as the X-ray source. The signal was recorded for 2θ = 0.5 – 10 ° with a step of 0.02 °.s^{-1} at low angles, and for 2θ = 10 – 70 ° with a step of 0.02 °.s^{-1} at wide angles.

Specific surface area, pore size distribution and pore volume were obtained from nitrogen adsorption/desorption experiments. A known mass of sample were first degassed at 150 °C under 1.33 Pa overnight. Isotherms were collected at -196 °C on a Micromeritics Tristar equipment.

The specific surface area of the samples was determined using the linear part of the BET plot and the pore size was estimated using the desorption branch of the isotherms using the Barrett – Joyner – Halenda (BJH) model although it is well known that this method gives an underestimated pore size and that some new methods have been developed[54], we use it here for the sake of simplicity and the use of this mathematical algorithm does not affect significantly our results as it is a systematic comparison. The microporous volume is extrapolated from the linear part of the t-plots

The Raman spectroscopic measurements were performed at room temperature with a FRA106/S FT-Raman module attached to a Bruker Equinox 55 FT-IR spectrometer equipped with a Nd:YAG laser operating at 1064 nm and a Ge detector. The spectra were collected using an output laser power of 400 mW and a spectral resolution of 4 cm^{-1}.

Diffuse reflectance UV-Vis spectra were obtained in air and under ambient conditions using a Lambda Perkin-Elmer spectrometer equipped with an integrated sphere for solid samples. The quantity of crystallized anatase (wt%) in each sample was determined by XRD quantification using an internal standard. The reflexion (2 0 0) at 48.04 °2θ has been chosen for the study because it corresponds to the first most intense and isolated peak, which is not in the region of the amorphous SiO_2 signal. The internal standard chosen is α-Al_2O_3 (corundum, Fluka) due to the presence of an intense peak (reflexion (1 1 3) at 43.35 °2 θ) close to the studied one on anatase XRD pattern with no possible overlapping (Fig. S1).

Physical mixtures of anatase 10 nm (Alfa Aesar) and calcined SBA-15 (series a aged at 130 °C) have been prepared in order to make standard compositions. For each XRD pattern, recordings were made at constant mass and volume, in the following mass proportions: 1/3 internal standard and 2/3 sample. A calibration line was made with the different standard mixtures at 10, 20, 40, 60, 80 and 100 wt% TiO_2 (Fig. S2).

Photocatalytic activity

Methyl orange (MO) was chosen as the organic compound to evaluate the photocatalytic properties of the different nanocomposites synthesized. Analyses have been performed according to the previously published procedure[32]. 50 mg of composite (or commercial anatase 10 nm purchased from Alfa Aesar, or P25 from Evonik) have been added to 100 mL of an aqueous MO solution (16 mg L^{-1}). The reaction was carried out under continuous stirring in a quartz

flask. The resulting suspension was left 1h in the dark to equilibrate the system prior irradiation. The UV-VIS spectra of the initial MO solution and the suspension prior irradiation are similar indicating that no MO was adsorbed on the catalyst.
Samples were irradiated with UV light from a high-mercury lamp. The irradiation was assured by artificial light using a mercury lamp (low pressure mercury arc, USHIO, light power 7 W) emitting in the near-UV. The mean value of the radiation power impinging on the reacting suspension was estimated to be $I_{incident}$ = 10^{-5} Einstein L^{-1} s^{-1}. The degradation process of MO was monitored using a Cary 3EG UV-Vis-spectrophotometer. The photocatalytic degradation of MO in solution was followed by measuring the absorbance value at λ = 464 nm, which allowed access to the MO concentration. Analytical uncertainty on MO concentration was mainly due to the filtration step (performed on the suspension MO aqueous solution/catalyst with YY filter) and has been evaluated to be 1.5 mg L^{-1}.

Results and discussion

SBA-15 host supports

The N_2 sorption isotherms of the different supports are reported in Fig. 1 and the corresponding textural properties are presented Table S1. Whatever the ageing temperature during the synthesis, the SBA-15 type OMS isotherms are all of type IV according to IUPAC classification[55].

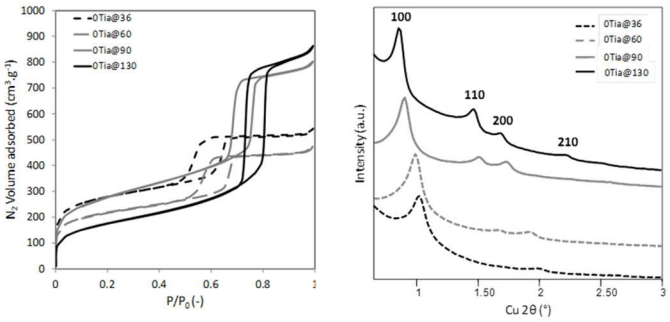


Fig. 1. N_2 adsorption – desorption isotherms (left) and low-angles X-ray diffraction patterns (right) of SBA-15 type mesoporous silicas synthesized after ageing at different temperatures.

The N_2 sorption isotherms of OMS synthesized at ageing temperature inferior or equal to 90 °C are also type I indicating the presence of microporosity. Indeed these materials are characterized by main cylindrical mesopores arranged in a 2D-hexagonal packing and micropores due to the interpenetration of PEO chain in the silica network. The SBA-15 host synthesized at 90 °C has also secondary small mesopores and/or supermicropores that interconnect primary mesopores. As a result, these materials present high specific surface area and large pore volumes. The SBA-15 host synthesized at 130 °C is characterized by large primary mesopores interconnected by secondary mesopores. The absence of micropores in this material explains in part the lower specific surface area. The XRD patterns obtained in the low 2θ region clearly show three diffraction peaks, characteristic of the (1 0 0), (1 1 0) and (2 0 0) diffraction planes of the 2D hexagonal pore structure (Fig. 1). This suggests samples having a well-ordered mesostructure. The corresponding lattice spacings estimated on the (1 0 0) diffraction peak are presented Table S1. As expected, according to Galarneau *et al.*[56], the pore diameter increases and so the silica walls thickness decreases (not presented here) when the ageing temperature increases. The SEM images of the different SBA-15 host supports are presented Fig. S3. In all cases, the SBA-15 presents a fiber-like morphology made by micron size rods of about 1 µm (length) and 200 nm (width).

TiO_2 – SiO_2 composites

By observing the SEM images of the composites of the series a (50 wt% of TiO_2), it appears that in the case of hosts aged at temperature ≥ 90 °C the rod-shape morphology of SBA-15 particles is still observed (Fig. 2C, D). In the case of hosts aged at lower temperatures (36 and 60°C) the rod-shape morphology is still present but particles with undefined morphology are also observed (Fig. 2A, B).
The proportion of these latter increase with decreasing of the ageing temperature. These changes in morphology can be explained by the formation of TiO_2 outside SBA-15 hosts or by textural modification upon TiO_2 crystallization.

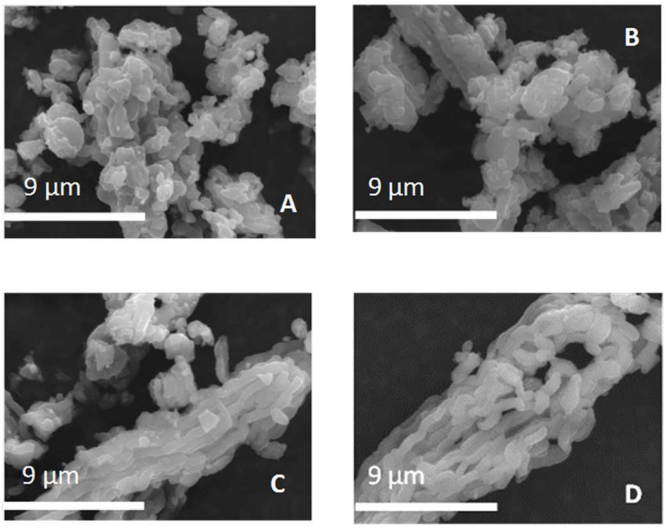


Fig. 2. SEM images of the 50 wt% TiO_2 – SiO_2 composites (series a) obtained from SBA-15 aged at different temperatures.

For the composites of series b, the fibre morphology of aggregates and the rod-shape morphology of primary SBA-15 particles is observed for TiO_2 contents ≤ 50 wt% (Fig. 3A, B, C).

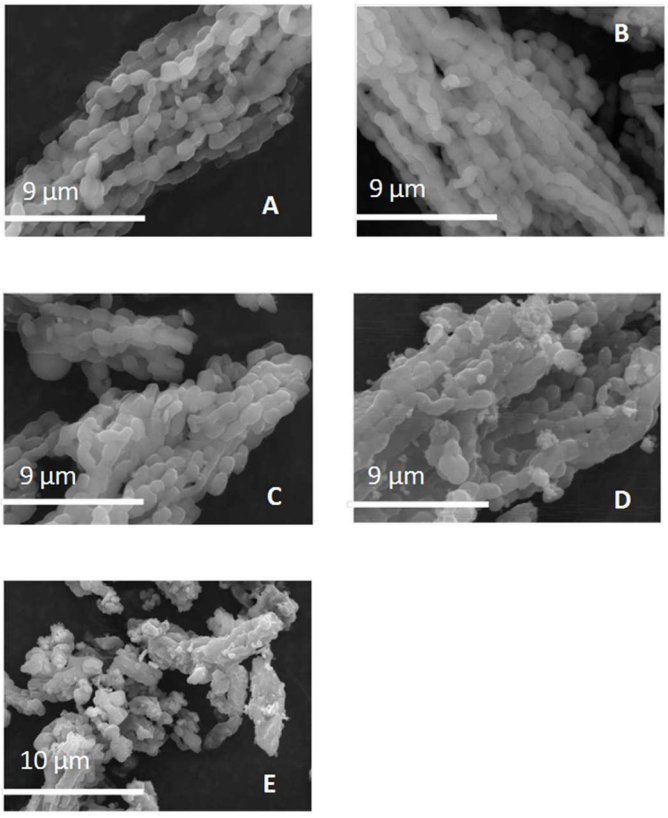


Fig. 3. SEM images of the TiO_2 – SiO_2 composites obtained from SBA-15 aged at 130 °C (series b) with 10 wt% (A), 25 wt% (B), 50 wt% (C), 70 wt% (D) and 80 wt% (E) of TiO_2.

Some morphology changes were observed when increasing the TiO_2 content (> 50 wt%). For 70Tib@130 rod-like particles are still observed and in major proportion, but other particles with undefined particles are also observed (Fig. 3D). For 80Tib@130, the rod-like morphology is barely observed and major particles have undefined morphology corresponding to TiO_2 formation outside the SiO_2 host (Fig. 3E). As suggested for the composites of the series a obtained from hosts aged at low temperatures, the crystallization of TiO_2 under thermal treatment at 400 °C has provoked structural and textural modifications leading to a slight modification of the silica host morphology.

However the rod-shape morphology of SBA-15 particles is globally preserved as observed by TEM (fig. SI). The difficulty to observe them is due to the low SiO_2 content compared to the high TiO_2 content.

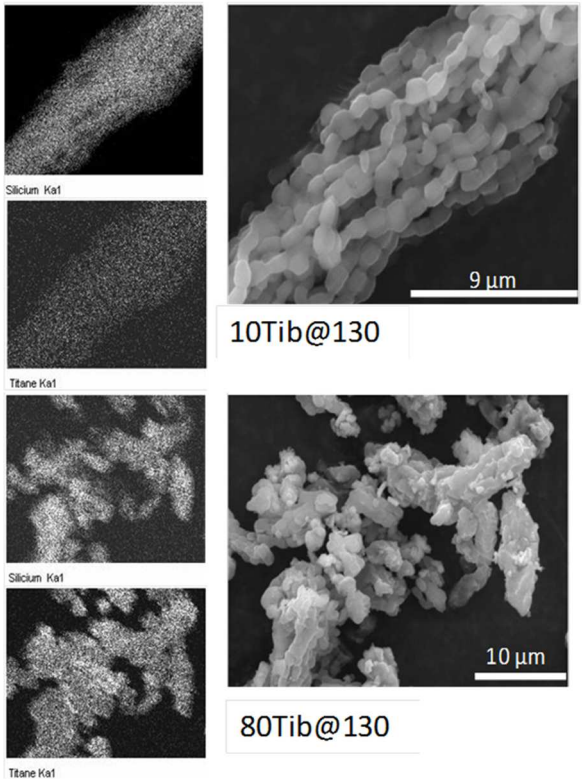


Fig. 4. SEM and corresponding elemental mapping images of 10Tib@130 and 80Tib@130.

It cannot be excluded that some particles with undefined morphology correspond to the outside formation of TiO_2 particles. The elemental mapping images displayed in Fig. 4 show the repartition of Ti and Si in some composites. In the case of 10Tib@130, the Ti signal is low due to the small quantity of TiO_2 in the composites. Whatever the TiO_2 content, it seems that the impregnation method used allows a homogeneous repartition of TiO_2 on the SiO_2 supports. However the low resolution of the elemental mapping does not allow to distinguish individually the particles and to check if the ratio Ti/Si is constant or variable from one particle to another one.

The N_2 adsorption - desorption isotherms of the two series of composites are displayed in Fig. 5. By focusing on the composites of the series a, all isotherms are type IV, but compared to the SBA-15 hosts, the condensation capillary steps are broader due to a larger pore size distribution and the hysteresis are type H2[55] indicating a partial pore blocking. The shape of the isotherms is in agreement with the partial filling of main mesopores. The fast desorption at P/P_0 of 0.45 corresponds to the catastrophic emptying of mesopores characteristics of bottle-necked pores. The average pore size measured from the desorption branch is then non indicative. However it is interesting to note that the condensation capillary step on the adsorption branch occurs at lower P/P_0 indicating lower pore sizes than those of the corresponding SBA-15 hosts. These results show that some TiO_2 are inside primary mesopores forming bottlenecks.

Concerning the isotherms of the series b, they are all type IV with H1 type hysteresis[55] but with different shapes from parent SBA-15 hosts at high TiO_2 contents. By comparing the shapes of the isotherms of the composites 10Tib@130 and 25Tib@130 to the host SBA-15 aged at 130 °C, the same hysteresis of H1 type is observed with a high and thin capillary condensation step.

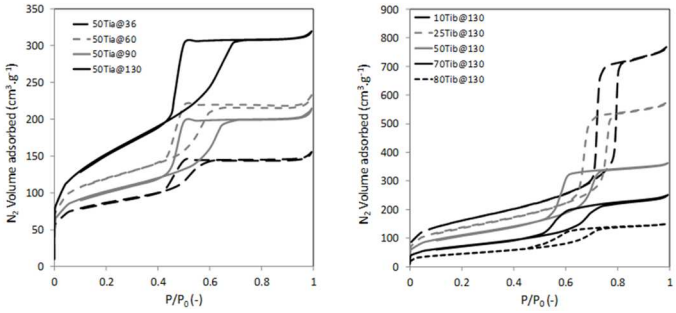


Fig. 5. N_2 adsorption – desorption isotherms of the composites.

In these cases it seems that TiO_2 is homogeneously located on the pore surface or outside of the pores, this is in agreement with results reported in the literature indicating that a loading of 20 wt% of TiO_2 is the optimal value for an homogenous dispersion[37]. The first case is the most probable since the morphology of particles observed by SEM is very similar to the one of the SBA-15 hosts. When increasing TiO_2 content (≥ 50 wt%), the shape of the isotherms change with decreasing and broadening of the capillary condensation step corresponding to larger pore size distributions and decreasing of the mesopore volumes. The textural characteristics of all composites are reported Table 1. For composites of the series a (50 wt% TiO_2), it clearly appears that the specific surface area and the pore volumes are lower than those of the host supports. The decrease is more pronounced for composites obtained from a SBA-15 host synthesized at low ageing temperatures (≤ 90°C). This is due to the presence of microporosity which is low, indicating a partial micropore filling in the composites. For 50Tia@130, both decrease of the specific surface area and micropore volume is low but the decrease of the mesopore volume is high compared to the SBA-15 host. This means that the pore size of the silica supports, aged at 130 °C is large enough (about 8 nm) to allow the impregnation inside the mesoporosity.

Table 1. Structural and textural properties of the different composites

Sample	S_{BET}[a] / $m^2.g^{-1}$	V_{mes}[a] / $cm^3.g^{-1}$	V_{micro}[a] / $cm^3.g^{-1}$	Dp[a] / nm	a_0[b] / nm
50Tia@36	311	0.16	0.06	3.7	9.2
50Tia@60	424	0.25	0.08	3.4	9.7
50Tia@90	362	0.25	0.06	4	10.3
50Tia@130	537	0.44	0.04	3.8	11.1
10Tib@130	580	1.10	0.03	7.6	11.5
25Tib@130	495	0.83	0.02	6.3	11.4
50Tib@130	397	0.52	0.01	4.9	11.2
70Tib@130	261	0.36	0.00	4.6	11.1
80Tib@130	163	0.21	0.00	4.3	-

[a] S_{BET} is the specific surface area obtained using the BET model, V_{micro} is the microporous volume extrapolated from the t-plots, $V_{meso} = V_{tot} - V_{micro}$ is the mesopore volume where V_{tot} is the total pore volume obtained at $P/P_0 = 0.9$, D_p is the mean pore diameter obtained using the BJH model on the desorption branch.

[b] a_0 is the lattice parameter calculated for a 2D hexagonal system, $a_0 = (2d_{100})/\sqrt{3}$, where d_{100} is the lattice spacing obtained using low angle XRD

For the series b of composites prepared from the SBA-15 type OMS aged at 130 °C, the specific surface area, the pore volume and pore diameter decrease when increasing the TiO_2 content. Surprisingly, the specific surface area of the composite 10Tib@130 is higher than the one of the corresponding host. This composite displays also microporosity (micropore volume of 0.03 $cm^3\ g^{-1}$ with a micropore specific surface area of about 70 $m^2\ g^{-1}$ determined by the t-plot method) which is not the case of its host. This microporosity can explain the increase of the specific surface area. The presence of microporosity is also observed for composites with 25 and 50 wt%, and is probably attributed to the formation of nanodomains of TiO_2 inside mesopores and/or on the surface of SBA-15 particles with most probably intergrain microporosity.

The comparison of the N_2 sorption data of the two series show that TiO_2 is more homogeneously dispersed in series b indicating that the presence of large mesopores is more favourable for the impregnation method used.

For the composites of series a prepared with 50 wt% of TiO_2, the low angles XRD patterns exhibit the (1 0 0) diffraction peaks of the host supports in all cases. Compares to those of the host silica materials, the (1 0 0) peaks of corresponding composites are shifted to higher angles as a result of a network contraction upon the thermal treatment at 400 °C. The absence of the other reflexions is indicating of the loss of ordering probably due to the crystallization of TiO_2 during the thermal treatment at 400 °C. At wide angles, peaks corresponding to crystallized anatase (ICDD n°03-065-5714) are observed for composites prepared with SBA-15 aged at temperatures below 130 °C (Fig. 6).

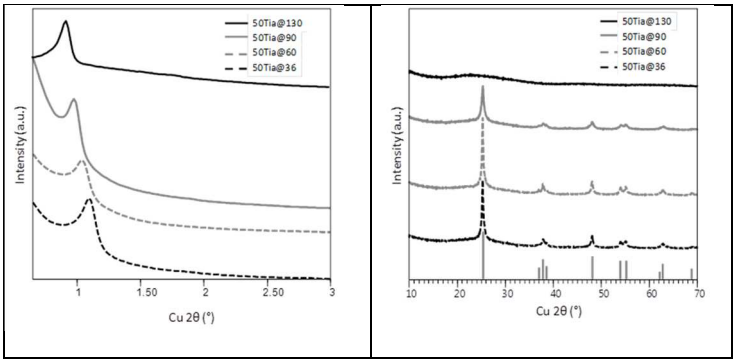


Fig. 6. Low (left) and wide (right) angles XRD patterns of the composites at 50% TiO_2 content.

The absence of crystalline anatase on the XRD pattern of 50Tia@130 suggests that due to the large pores of the host, TiO_2 is entirely inside the porosity. According to the SEM images, the shape of N_2 adsorption/desorption isotherms and XRD data it seems that with the SBA-15 aged at temperatures below 130 °C, the impregnation is both inside and outside the porosity where crystallized anatase is visible. By XRD Scherrer method, an average crystal size of 32, 43 and 18 nm is obtained for the composites with the supports aged at 36, 60 and 90 °C, respectively (Table 2). The crystal size is obviously much larger that the pore size confirming that anatase crystallized outside the SBA-15 host pores. By XRD quantification, the materials exhibit 19 wt% of anatase for 50Tia@90 and 22 wt% of anatase for 50Tia@36 and 50Tia@60. As no anatase reflection is visible for 50Tia@130 (Fig. 6), no quantification could be done. The results of anatase quantification and anatase crystal sizes of the different composites are summarized in Table 2.

Table 2: Crystal sizes and anatase quantity in the different composites with crystallized TiO_2

Sample	Crystal size[a] / nm	Anatase quantification[b] / wt%
50Tia@36	32	22
50Tia@60	43	22
50Tia@90	18	19
50Tib@130	8	15
70Tib@130	13	28
80Tib@130	23	44

[a] average crystal size obtained using XRD Scherrer method
[b] anatase quantification obtained by method described in the experimental part

Raman spectra of the composites of series a are presented Fig. 7. A reference sample of anatase 10 nm was used in order to compare it to the different composites.

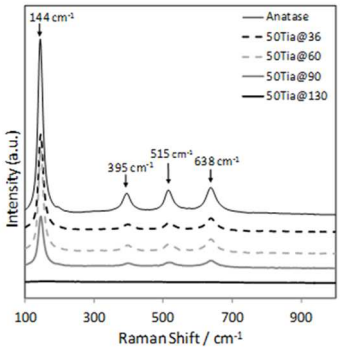


Fig. 7. Raman spectra of the composites of series a (50 wt% of TiO_2).

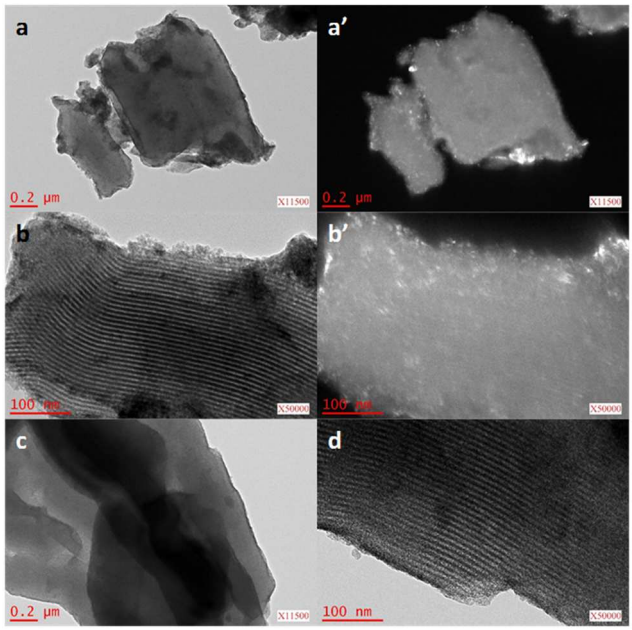


Fig. 8. TEM images of composites of series a: (a,a',b,b') 50Tia@36 and (c,d) 50Tia@130.

The four different bands at 144, 395, 515 and 638 cm^{-1}, assigned to crystallized anatase are visible for anatase 10 nm and all composites except for 50Tia@130. These results confirm that no crystallized anatase is present in 50Tia@130 sample. Composites of series a have been observed by TEM (Fig. 8 and S4). For each sample, the corresponding image obtained by dark field method is presented, allowing to bring out the crystallized TiO_2 particles. No visible crystallized particle is visible in 50Tia@130, which is in agreement with the results obtained by wide-angle XRD and Raman. For all samples, the lattice fringes corresponding to the packing of cylindrical mesopores of the silica SBA-15 hosts are clearly observed. In the case of 50Tia@36 and 50Tia@60, aggregates of particles of about 5nm in diameter are also observed on the surface of rod-shape SBA-15 particles (Fig. 8b). These particles are probably TiO_2 particles formed under thermal treatments at 400 °C. These observations are in agreement with SEM observations showing particles with undefined morphology. The TEM images with dark field mode show that crystalline anatase particles are well dispersed with a major proportion on the SBA-15 particle surface.

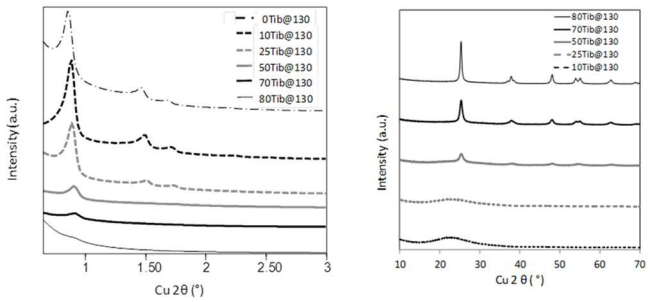


Fig. 9. Low angles (left) and wide angles (right) XRD patterns of the catalysts with different TiO_2 content (series b).

Fig. 9 presents low- and wide-angle XRD patterns of these composites. For all composites at least the reflexion (1 0 0) is observed on low-angle XRD patterns. The (1 1 0) and (2 0 0) are also clearly observed for the composites with low TiO_2 contents, 10Tib@130 and 25Tib@130. However, these two reflexions are not observed at higher TiO_2 content (≥ 50 wt%), while they are clearly observed for a physical mixture of silica SBA-15 with crystalline anatase (50 wt%) (Fig. S5).

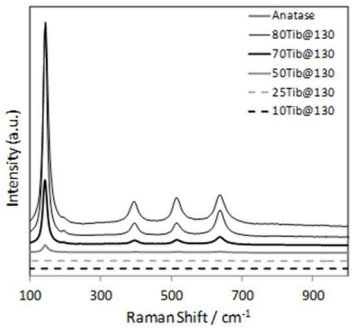


Fig.10. Raman spectra of the composites of series b

This confirms that at high TiO_2 contents the crystallisation of TiO_2 upon thermal treatment at 400 °C leads to significant structural changes. The decrease of the intensity of the reflexions is a consequence of the dilution of the silica SBA-15 matrix with TiO_2. The presence of crystallized anatase in the composites from 50 wt% of TiO_2 content is evidence by wide-angle XRD and Raman spectroscopy (Fig. 9 and 10). It is noteworthy that contrary to 50Tia@130, the composite 50Tib@130 presents some crystallized anatase. This can be explained by the small differences observed in textural properties of the two host supports used (Table 1). These differences reveal some problems of repeatability due to uncontrolled experimental parameters such as the addition way of SiO_2 and TiO_2 precursors and the room temperature during impregnation.

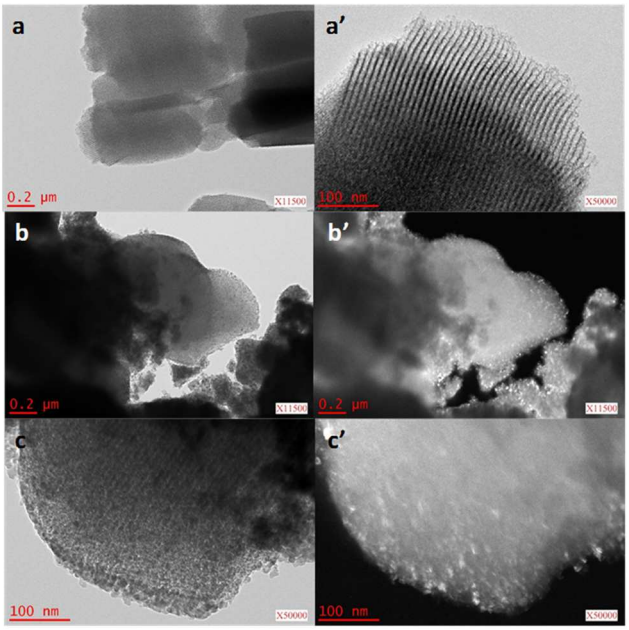


Fig. 11. TEM images of composites of series b: (a,a') 10Tib@130 and (b,b',c,c') 70Tib@130

The presence of crystallized anatase in composites with 50, 70 and 80 wt% TiO_2 content is confirmed by TEM images with dark field mode presented Fig. 11 and S6. There is no TEM images in dark field mode for 10Tib@130 and 25Tib@130 because no crystallized anatase is present in both samples, which is consistent with XRD and Raman results. For all samples, particles with rod-shape morphology and lattice fringes characteristics of the 2D-hexagonal pore network characteristic of the SBA-15 hosts are clearly observed. Like for 50Tia@36 and 50Tia@60, small 5-nm particles more or less aggregated are also observed on the SBA-15 particle surfaces of 50Tib@130, 70Tib@130 and 80Tib@130. These observations are consistent with SEM observations. Anatase crystallites look homogeneous in size and homogeneously dispersed inside or outside the silica SBA-15 hosts. The crystal sizes measured by XRD Scherrer method on the samples are 8, 13 and 23 nm for the samples containing 50, 70 and 80 wt% of TiO_2, respectively (Table 2).

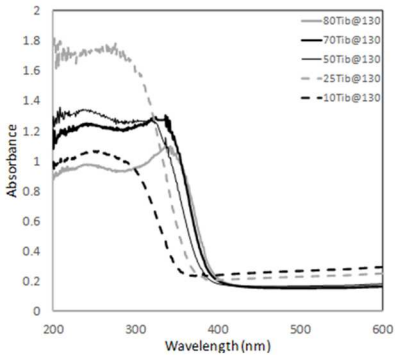


Fig. 12. DR UV-Vis spectra of the series b composites.

When increasing the TiO_2 content, the impregnation and the crystallization of TiO_2 takes place inside and outside the porosity. By XRD quantification the materials exhibit 15, 28 and 44 wt% of crystallized anatase for 50, 70 and 80 wt% of TiO_2 content, respectively.

Fig.12 shows the DR spectra of the different composites of series b. For 50, 70 and 80 % of TiO_2.The adsorption occurs in a range between 230 and 400 nm. They exhibit a broad band that can be decomposed in two parts. The first contribution at around 250 nm arises from a ligand to metal charge transfer transition in isolated TiO_4 units. It corresponds to coordinated Ti^{4+} species that are incorporated into the silica framework. The second contribution at 350 nm corresponds to small TiO_2 clusters. A blue shift is observed when the titania content drecreases meaning that the size of the particles is reduced. This blue shift has been observed for titania nanopaticles[57,58] on silica and corresponds to small TiO_2 clusters through the quantum size effect. These observations support the XRD results, i.e. an increase of the particles' size as a function of the TiO_2 content.

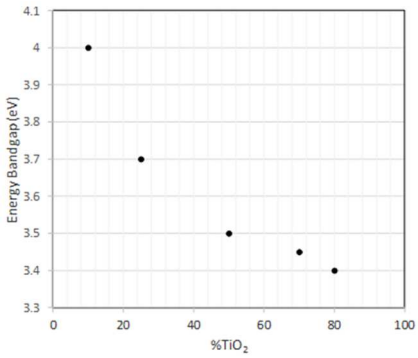


Fig. 13. Evolution of the energy band gap of the composites according to the TiO_2 content.

Using the Kubelka-Munk function, the band gap (Eg) has been calculated from a plot of $(\alpha h\nu)^2$ versus photon energy ($h\nu$), where α stands the adsorption coefficient. The band gap is determined by extrapolating the straight line portion of $(\alpha h\nu)^{1/2} = 0$ axis.The intercept of the tangent of the plot gives the value of E (Fig S6). The bang gap decreases from 4.0 to 3.4 eV, when the TiO_2 content is increased from 10 to 80% (Fig. 13). Thus, with the increase of the tinania content Eg is near the value of the pure anatase 3.2 eV. This result is in accordance with the ones obtained by XRD. Indeed it should be reminded that an increase of the anatase content in the composite is noted with when the TiO_2 content varies from 10 to 80%.

Photocatalysis experiments

Fig. 14 shows the photocatalytic results obtained using the catalysts of the series a compared to commercial anatase 10 nm and P25. P25 appears to be the best photocatalyst with a total degradation of MO after 90 min of irradiation time. With the host support aged at 130 °C the MO degradation is less important, only 20 % of degradation is observed after 150 min. This sample also corresponds to the one for which no crystallisation of anatase was observed. For the other samples, the degradation profile is quite similar which can be explained by the presence of almost the same crystallized anatase amount (around 20 wt%).

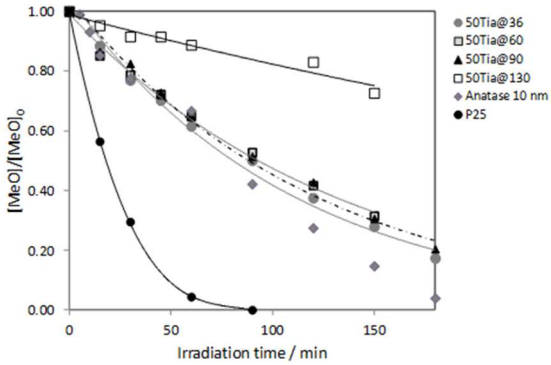


Fig. 14. Evolution of MO concentration with irradiation time by using the different catalysts at 50 wt% of TiO_2 (series a) and two commercial references.

Compared to the sample of anatase 10 nm, the profiles of the samples at 50 wt% of TiO_2 using SBA-15 host support aged at temperature inferior to 130 °C are quite similar until 90 min of reaction.

After that, the anatase 10 nm exhibits a better activity than the composites. The evolution of the MO concentration with the irradiation time using the samples at different TiO_2 contents prepared from SBA-15 silica aged at 130 °C (series b) as photocatalysts, is presented Fig. 15. In this case, it clearly appears that the degradation of MO using samples with low TiO_2 content (10 and 25 wt%) is quite low and slow. This is consistent with the absence of any crystallized anatase observed by wide-angle XRD. The necessity of having crystallized anatase particle is evidenced here, by comparing 50Ti@130 of both series (Fig. 14 and 15), the photoactivity is improved in the second case (series b – Fig. 15) when crystallized particles are present in the composite. Moreover, it seems that the degradation of MO is improved by increasing the TiO_2 content (Fig. 15). No relevant difference is observed between the samples with 70 or 80 wt% of TiO_2 but their photoactivity is very similar to that of anatase 10 nm. These results are interesting, because in that case, although there is 70 or 80 wt% of TiO_2 due to the impregnation method, only a part of it had crystallized in anatase resulting in 28 and 44 wt % of anatase, respectively, with particle size of about 13 and 23 nm, respectively.

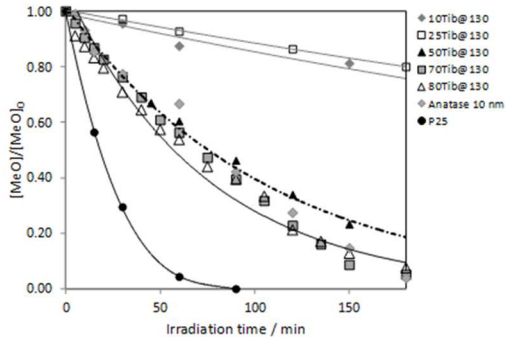


Fig. 15. Evolution of MO concentration with irradiation time by using the different catalysts at different wt% of TiO_2 (series b) and two commercial references.

It is noteworthy that the commercial anatase 10 nm is totally crystalized (100 wt%). Anatase nanocrystals appear thus more efficient photocatalysts when they are dispersed in silica matrices with high specific surface areas. However, P25 appears to be the best catalyst for the MO degradation in our conditions. The unusually high photocatalytic activity of the TiO2 P25 is attributed to the complex structure of this material since it is a mixture of anatase crystallites with amorphous and rutile phases. For nanoparticles (such as P25), the transportation length of electron/hole from crystal interface to the surface is short, which helps to accelerate the migration rate of electron/hole to the surface of the nanoparticle to participate the reaction process[59]. The commercial anatase 10 nm and 80Tib@130 are then the following best catalysts. But although, anatase 10 nm is better at the beginning of the degradation of MO, the composite 80Tib@130 tends to follow the same profile of anatase 10 nm after 100 min of irradiation, which confirms that with less crystallized anatase in the catalyst (44 wt%), the composite exhibits a photocatalytic activity close to the fully crystallized anatase one.

The effect of the anatase concentration on the degradation rate of MO is evaluated Fig. 16. The rates are determined at 60 min after the initiation of the photocatalytic activities. This reaction time is high enough to obtain different values for the degradation rates under different conditions. The catalyst loading is the same for each experiment in order to avoid the photodegradation activitiy variations that can be observed[60].

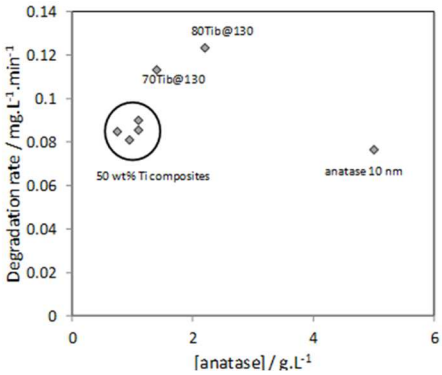


Fig. 16. Effect of the anatase content in the composites on the rate of degradation of MO.

By observing Fig. 16, it appears that anatase 10 nm sample and composites at 50 wt% of TiO_2 exhibit equivalent rates of degradation of MO. In the first case, anatase 10 nm exhibits 100 % of crystallized anatase whereas the 50 wt% composites exhibit around 20 % of crystallized anatase for the same quantity of catalyst. At this stage, the composites at 50 wt% composites exhibit identical rate degradation with lower crystallized anatase. These composites are clearly more efficient than anatase 10 nm. Moreover It is worth mentioning the important degradation rates obtained by the composites with 70 and 80 wt% of TiO_2, that are higher than the one with fully crystallized sample and the best degradation rate was observed using 80Tib@130 composite. In this case, the degradation rate of 80Tib@130, composite exhibiting 44 % of anatase, is twice better than the anatase 10 nm one where the sample is 100 % crystallized. It clearly appears that the composites synthesized in this study are better photocatalysts, when crystallized anatase is formed during calcinations, than fully crystallized anatase.

Conclusions

Two different series of composites were synthesized by post-impregnation of a SBA-15 host support. In series a, the influence of the pore size of the silica supports on the dispersion of TiO_2 was evidenced. Four different OMS were prepared with different ageing temperature: 36 °C, 60 °C, 90 °C and 130 °C. In order to allow a quasi-total impregnation inside the porosity, an ageing at 130 °C is necessary, leading to SBA-15 with large mesopores of about 8 nm.

In series b, SBA-15 aged at 130 °C is used as host support and the TiO_2 content of the composites is varied. In this case, it seems that the impregnation occurs both inside and outside the porosity, and that TiO_2 crystallized in anatase phase outside the porosity. At low TiO_2 content ≤ 25wt% the impregnation occurred homogeneously inside the mesopores but no crystalline anatase was observed by XRD and Raman.

The use of SBA-15 host support with large mesopores, compared to those used in series a, allows a better dispersion of TiO_2 particles. The quantity of crystallized anatase was determined by XRD using an internal standard when crystalline particles were visible. For these composites, the initial quantity of TiO_2 varied from 50 to 80 wt% with different quantity of crystallized anatase from 15 to 44 %, respectively.

The photocatalytic activity of the composites was evaluated by following the degradation of MO and compared to commercial references. While P25 sample appeared to be the best photocatalyst for the degradation of MO in our conditions, the photoactivity of the other composites exhibiting crystallized anatase were similar to that of fully crystallized anatase. However by comparing the degradation rate of MO using all the other composites, it clearly appears that 80Tib@130 with only 44 wt% of crystallized anatase, exhibits the highest MO degradation rate of both series.

† Electronic Supplementary Information (ESI) available: XRD patterns of the anatase phase and the internal standard chosen (S1). Calibration line obtained with the standard mixtures (S2). SEM images of the SBA-15 type ordered mesoporous silicas aged at 36 °C (A), 60 °C (B), 90 °C (C) and 130 °C (D) (S3). TEM images with bright and dark field mode of 50Ti-Si60a (left) and 50Ti-Si90a (right) (S4). Low-angles XRD patterns of a physical mixture (50 wt% of TiO_2 and SBA-15) and the composite 50Ti-Si130b (S5). TEM images with bright and dark field mode of 25Ti-Si130b (left) and 80Ti-Si130b (right) (S6). See DOI: 10.1039/x0xx00000x

Acknowledgements

Issam Naboulsi is warmfully thanked for his help in photocatalysis experiments. Habiba Nouali and Ludovic Josien are thanked for the analyses made on the platforms (certified ISO9001) Adsorption and Electronic Microscopy, respectively, of IS2M.

References

1 J.M. Hermann, *Top. Catal.*, 2005, **34**, 49.
2 U.I. Gaya and A.H.Abdullah, *J. Photochem. Photobiol. C: Photochem. Rev.*, 2008, **9**, 1.
3 M. Andersson, L. Osterlund, S. Ljungstrom and A. Palmqvist, *J. Phys. Chem. B*, 2002, **106**, 10674.
4 X. Chen and S.S. Mao, *Chem. Rev*., 2007, **107**, 2891.
5 A. Fujishima, X. Zhang and D. A. Tryk, *Surf. Sci. Reports*, 2008, **63**, 515.
6 E. Pelizzetti, C. Minero, E. Borgarello, L. Tinucci and N. Serpone, *Langmuir,* 1993, **9**, 2995.
7 B. Ohtani, Y. Ogawa and S. Nishimoto, *J. Phys. Chem. B*, 1997, **101**, 3746.
8 Z. Li, B. Hou, Y. Xu, D. Wu and Y. Sun, *J. Colloid Interface Sci.*, 2005, **288**, 149.
9 D.S. Kim, S.J. Han and S.Y. Kwak, *J. Colloid Interface Sci.*, 2007, **316**, 85.
10 G. Xu, Z. Zheng, Y. Wu and N. Feng, *Ceramics Inter*., 2009, **35**, 1.
11 M. Harada, T. Sasaki, Y. Ebina and M. Watanabe, *J. Photochem. Photobiol. A: Chem.*, 2002, **148**, 273.
12 J. Chen, F. Qiu, W. Xu, S. Cao and H. Zhu, *Appl. Catal. A: General*, 2015, **495**, 131.
13 M. Bonne, S. Pronier, Y. Batonneau, F. Can, X. Courtois, S. Royer, P. Marécot and D. Duprez, *J. Mater. Chem.*, 2010, **20**, 9205.
14 D.J. Reidy, J.D. Holmes and M.A. Morris, *Ceramics Inter.*, 2006, **32**, 235.
15 K. Zimny, J. Ghanbaja, C. Carteret, M.J. Stébé and J.L. Blin, *New J. Chem.*, 2010, **34**, 2113.
16 K. Zimny, C. Carteret, M.J. Stébé and J.L. Blin, *J. Phys. Chem. C*, 2012, **116**, 6585.
17 K. Assaker, T. Benamor, L. Michelin, B. Lebeau, C. Marichal, M.J. Stébé and J.L. Blin, Microporous Mesoporous Mater., 2015, **201**, 43.
18 R. Zhang, A.A. Elzatahry and S.S. Al-Deyab, *Nano Today*, 2012, **7**, 344.
19 C. Galacho, M.M.L. Ribeiro Carrott and P.J.M. Carrott, *Microporous Mesoporous Mater.*, 2007, **100**, 312.
20 G. Li and X.S. Zhao, *Ind. Eng. Chem. Res.*, 2006, **45**, 3569.
21 J.A. Melero, J.M. Arsuaga, P. De Frutos, J. Iglesias, J. Sainz and S. Blázquez, *Microporous Mesoporous Mater.*, 2005, **86,** 364.
22 W.-H. Zhang, J. Lu, B. Han, M. Li, J. Xiu, P. Ying and C. Li, *Chem. Mater.*, 2002, **14**, 3413.
23 Y. Chen, Y. Huang, J. Xiu, X. Han and X. Bao, *Appl. Catal., A*, 2004, **273**, 185.
24 M.D. Alba, Z.H. Luan and J. Klinowski, *J. Phys. Chem.*, 1996, **100**, 2178.
25 J. Li, C. Zhou, H. Xie, Z. Ge, L. Yuan and X. Li, *J. Nat. Gas Chem.*, 2006, **15**, 164.
26 F. Bérubé, B. Nohair, F. Kleitz S. Kaliaguine, *Chem. Mater.*, 2010, **22**, 1988.
27 N.B. Lihitkar, M.K. Abyaneh, V. Samuel, R. Pasricha, S.W. Gosavi and S.K. Kulkarni, *J. Colloid. Interface Sci.*, 2007, **314**, 310.
28 S.G. Zhang, Y. Fujii, H. Yamashita, K. Koyano, T. Tatsumi .and M. Anpo, *Chem. Lett.*, 1997, **26**, 659.
29 T. Maschmeyer, F. Rey, G. Sankar and J.M. Thomas, *Nature*, 1995, **378**, 159.
30 K. Yamagishi, S. Namba and T. Yashima, *Stud. Surf. Sci. Catal.*, 1991, **60**, 171.
31 G. Li, and X.S. Zhao, *Ind. Eng. Chem. Res.*, 2006, 45, 3569.
32 J.L. Blin, M.J. Stébé and T. Roques-Carmes, *Colloids Surf. A Physicochem. Eng. Asp.*, 2012, **407**, 177.
33 K. Assaker, C. Carteret, T. Roques-Carmes, J. Ghanbaja, M.J. Stébé and J.L. Blin, *New J. Chem.*, 2014, **38**, 2081.
34 M. Bellardita, M. Addamo, A. Di Paola, L. Palmisano, L. Cassar and M. Borsa, *J. Hazard. Mater.*, 2010, **174**, 707.
35 T. Cetinkaya, L. Neuwirthová, K.M. Kutláková and V. Tomášek, *Appl. Surf. Sci.*, 2013, **279**, 384.
36 K.Y. Jung and S.B. Park, *Appl. Catal. B: Environment.*, 2000, **25**, 249.
37 M.T. Nguyen Dinh, P. Rajbhandari, C. Lancelot, P. Blanchard, C. Lamonier, M. Bonne, S. Royer, F. Dumeignil and E. Payen, *ChemCatChem*, 2014, **6**, 328.
38 A. Corma, M.T. Navarro and J. Perez-Pariente, Patent 930 132 7 1993,
39 A. Corma A, M.T. Navarro and J. Perez-Pariente, *J Chem Soc. Chem. Commun,* 1994, **2**, 14718.
40 M. Morey, A. Davidson and G. Stucky, *Microporous Mater.*, 1996, **6**, 99.
41 D.Y. Zhao, Q.S. Huo,J.L. Feng, B.F. Chmelka and G.D. Stucky, *J Am Chem Soc.*, 1998, **120,** 6024.
42 P.T. Tanev, M. Chibwe and T.J. Pinnavaia, *Nature,* 1994, **368**, 321.
43 A. Tuel and L.G. Hubert Pfalzgraf, *J. Catal.*, 2003, **217**, 343.
44 F. Chiker, J. Ph Nogier, F. Launay and J.L. Bonardet, *Appl. Catal. A*, 2003, **243**, 309.
45 Z. Luan, J.Y. Bae and L. Kevan, *Microporous Mesoporous Mater.*, 2001, **48**, 189.
46 M.V. Landau, L. Vradman, X. Wang and L. Titelman, *Microporous Mesoporous Mater.*, 2005, **78**, 117
47 A.A. Ismail and D.W. Bahnemann, *J. Mater. Chem.*, 2011, **21**, 11686.
48 J. Hazard. materials B, 2006, **137**, 952.
49 Materials Sc. Engin. C, 2009, **29**, 1498.
50 Microporous Mesoporous Mater., 2006, **96**, 255.
51 Catal. Today, 2005, **101**, 307.
52 ChemSus Chem
53 D. Zhao, J. Feng, Q. Huo, N. Melosh, G.H. Fredrickson, B.F. Chmelka and G.D. Stucky, *Science*, 1998, **279**, 548.
54 C.P. Jarionec, M. Kruk and M. Jarionec, *J. Phys. Chem. B*, 1998, 102, 5503.
55 K.S.W. Sing, *Pure Appl. Chem.,* 1985, **57**, 603.
56 A. Galarneau, H. Cambon, F. Di Renzo, R. Ryoo, M. Choi and F. Fajula, *New J. Chem.*, 2003, 27, 73.
57 X. Gao, S.R. Bare, J.L.G. Fierro, M.A. Banares and I.E. Wachs, *J. Phys. Chem. B*, 1998, **102**, 5653.

58 B.J. Aronson, C.F. Blanford and A. Stein, *Chem. Mater.*, 1997, 2842.
59 D. Beydoun, R. Amal, G. Low and S. McEvoy, *J. Nanoparticle Res.*, 1999, **1**, 439.
60 J.L Blin, *Coll and surfaces A: Physisorption Eng Aspects*, 2012, **407**, 177.